nature communications

Article

https://doi.org/10.1038/s41467-025-58372-7

Nitrate reduction to ammonia catalyzed by GaN/Si photoelectrodes with metal clusters

Received: 30 September 2023

Accepted: 19 March 2025

Published online: 10 April 2025

Check for updates

Wan Jae Dong[1,2,4], Jan Paul Menzel[3,4], Kejian Li[1], Zhengwei Ye[1], Zhuoran Long[3], Ishtiaque Ahmed Navid[1], Ke R. Yang[3], Yixin Xiao[1], Victor S. Batista[3] ✉ & Zetian Mi[1] ✉

The development of photoelectrochemical cells for reduction of nitrate to ammonia under solar light is of significant interest for the production of clean chemicals and fuels but has remained a daunting challenge. Here, we investigate various metal catalysts supported on GaN nanowires grown on n^+-p Si wafer – an emerging functional platform for scalable artificial photosynthesis – and demonstrate highly stable and efficient photoelectrochemical nitrate reduction reaction. We find that Co and Ni catalysts on GaN/Si exhibit the best performance, with an onset potential >0.3 V_{RHE} and a faradaic efficiency of NH_3 of 99% at 0.2 V_{RHE}. These results highlight the advantage of photoelectrochemical system in achieving efficient nitrate reduction under more positive potentials. In-situ measurements and theoretical calculations reveal that the binding modes of the NO_2^- intermediate play a key role in the NH_3 synthetic process. These results demonstrate that the rational design of catalysts on photoelectrodes can construct synergistic metal-semiconductor interactions for efficient and stable photoelectrochemical NH_3 synthesis.

Nitrate (NO_3^-) is a common pollutant found in wastewater, industrial runoffs, and groundwater[1]. It represents a significant threat to human health since it induces diseases upon conversion to nitrite (NO_2^-) in the body[2,3]. The electrochemical NO_3^- reduction reaction (NO_3^-RR) is a promising method removing NO_3^- by producing ammonia (NH_3), a valuable fertilizer and industrial chemical. The NO_3^- RR is also an environment-friendly method to close the NO_3^-N cycle, reducing the need for the Haber-Bosch process which is energy-intensive and produces greenhouse gases[4–6]. From the energy perspective, it is advantageous when compared to NH_3 synthesis by N_2 reduction due to the lower dissociation energy of N=O bond (204 kJ/mol) of NO_3^- when compared to the N ≡ N bond (941 kJ/mol)[1,7]. NO_3^--to-NH_3 conversion in aqueous electrolyte is a complex 9-proton and 8-electron reduction reaction, where protons are provided by water dissociation. Therefore, the catalysts should have both activity for the water dissociation and the NO_3^- conversion to promote the NO_3^- RR[8]. In addition, the NO_3^--to-NH_3 reduction is a complicated reaction with different stages of intermediates having various binding modes. Electrocatalysts have been investigated for the NO_3^- RR, including metal nanoparticles (NPs)[9,10], alloys[11–13], and compounds[14–23], 2D materials[24], and single atom catalysts[25,26]. However, due to their limited functionality of catalyzing the water dissociation, NO_3^- activation, or reduction of intermediates to the NH_3, the overpotential still needs to be significantly improved for any practical consideration. In order to mitigate this issue, multiple functional sites for different catalytic reactions were integrated by decorating one catalyst onto another[18,27]. For instance, an electrocatalyst consisting of two phases of Cu/CuO_x and Co/CoO showed promising NH_3 synthetic performance due to efficient NO_3^--to-NO_2^- conversion on Cu/CuO_x and the subsequent NO_2^--to-NH_3 conversion on Co/CoO[18]. This synergistic relay catalysis or intermediate spillover improved the performance compared to their single phases.

Photoelectrodes, fabricated by coupling the catalysts with photo-responsive semiconductor, can convert solar energy directly to the

[1]Department of Electrical Engineering and Computer Science, University of Michigan, Ann Arbor, MI, USA. [2]Department of Integrative Energy Engineering, Graduate School of Energy and Environment (KU-KIST Green School), College of Engineering, Korea University, Seoul, Republic of Korea. [3]Department of Chemistry, Yale University, New Haven, CT, USA. [4]These authors contributed equally: Wan Jae Dong, Jan Paul Menzel. ✉e-mail: victor.batista@yale.edu; ztmi@umich.edu

chemical energy and further reduce the overpotential of the NO_3^- RR. Previously, Au-decorated Si nanowires (NWs) photoelectrode demonstrated photoelectrochemical (PEC) NO_3^- RR[28]. However, the maximum production rate of NH_3 (Y_{NH3}) was only ~0.4 μmol/h/cm^2 and the stability has remained very limited. Recent advancements in PEC NO_3^- RR using chalcogenide light absorbers demonstrated the potential of binary metal catalysts to enhance catalytic activity and efficiency. For instance, CuSn[29] and CoCu[30] catalysts integrated with Sb_2S_3 and Sb_2Se_3 photocathodes have shown exceptional faradaic efficiency of NH_3 (~97% at 0.4 V_{RHE} and 88% at −0.2 V_{RHE}, respectively) and low onset potentials (0.62 V_{RHE} and 0.43 V_{RHE}), highlighting their ability to optimize reaction kinetics and improve charge transfer efficiency. These studies illustrate the importance of catalyst design in achieving high performance in PEC NO_3^- RR systems.

When catalysts are decorated on the surface of semiconductors, the photoelectrodes have two or more different functional sites at the surface, leading to distinct electronic structures and unique catalytic activity. This determines the reaction thermodynamics, intermediate binding modes, and final products in various catalytic reactions, such as water splitting, carbon dioxide reduction, N_2 reduction, and NO_3^- reduction[31–36]. Recent studies have shown that GaN nanostructures, e.g., nanowires (NWs), inherently possess the excellent water dissociation activity due to characteristic Ga-N bond at the *m*-plane crystal facet[37–39]. This suggests that GaN NWs can be an ideal supporting materials to promote the proton-coupled electron transfer reaction including NO_3^- reduction to NH_3. If the integration of metal catalyst on the semiconductor nanostructures can demonstrate synergetic effects by reducing the thermodynamic energy barriers, controlling the binding modes of adsorbates, and providing a sufficient number of protons with effective transfer of photogenerated electrons, the photoelectrodes will further reduce the overpotential and enhance the productivity of NH_3 compared to electrocatalysts. Therefore, rational design of photoelectrodes by selecting a suitable catalyst on the semiconductor surface and the understanding of reaction pathways are urgently required to achieve more efficient and productive solar-driven NO_3^- conversion to NH_3.

In this work, we investigated the metal catalysts supported on GaN NWs vertically grown on n^+-p Si photoelectrodes for PEC NO_3^- RR to NH_3 to demonstrate the synergistic effects of metal catalysts and GaN NWs. We first screened various noble metals (Pt, Ir, Rh, Pd, Au, Ru, Ag) and transition metals (Cu, Ni, Co) on GaN NWs for NH_3 synthesis. Co-loaded GaN/Si (Co/GaN/Si) showed the highest faradaic efficiency of NH_3 ($FE_{NH3} > 90\%$) at the widest potential window (0.2 to −0.7 V_{RHE}). Ni/GaN/Si achieved the NH_3 production rate of 83.3 μmol/h/cm^2 and the maximum value of 201.6 μmol/h/cm^2 at potentials of 0 and −0.4 V_{RHE}, respectively. We characterized the performance of photoelectrodes based on the presence of GaN NWs and found that the catalysts loaded on GaN NWs showed much lower onset potential and higher productivity of NH_3 than those on planar n^+-p Si photoelectrodes. This is due to the synergetic metal-GaN interaction which enhances water dissociation and catalytic activity of nitrogen-containing intermediates. GaN NWs rapidly dissociate water, providing a sufficient number of protons near the surface, which in turn activates NO_3^- and facilitates its efficient conversion to NO_2^-. Then, following NO_2^- to NH_3 conversion is further promoted by catalysts. A series of in-situ experiments and theoretical calculations were performed to interpret reaction mechanisms and revealed that the binding modes of the NO_2^- intermediate (*ONO$^-$* or *NO_2^-) on the metal catalysts were the key to the further deoxygenation process. This work provides insights into the design of efficient photoelectrode for green NH_3 production.

Results

Metal catalysts loaded on GaN/Si photoelectrodes

Photoelectrodes were fabricated by plasma-assisted molecular-beam epitaxy growth of GaN NWs on n^+–p Si wafers, followed by photodeposition of metal catalysts on GaN NWs. A 45-degree tilt-view scanning electron microscopy (SEM) image of Co/GaN/Si showed that GaN NWs were vertically aligned on the n^+-p Si wafer, with a length of ~400 nm and diameter of ~50 nm (Fig. 1a). Since the particle size of metal catalysts was too small to be observed in the SEM image, we performed high-angle annular dark-field scanning transmission electron microscopy (HAADF-STEM) and energy-dispersive spectroscopy (EDS) elemental mapping to image the Co/GaN/Si (Fig. 1b and Fig. S1) and Ni/GaN/Si photoelectrodes (Fig. 1c and Fig. S2). The HAADF-STEM images showed the segregated Co and Ni nanoparticles (NPs) on both the top and sidewalls of GaN NWs. The atomic number difference between Co (27), Ni (28), and Ga (31) results in a Z-contrast that allows the NPs to be distinguished from the GaN NWs. The EDS elemental maps confirmed the presence of the metal catalysts, with locally aggregated Co (shown in yellow in Fig. 1b) and Ni (shown in orange in Fig. 1c). Ga (blue) and N (cyan) were uniformly distributed over the GaN NWs. The presence of oxygen indicates that the surface metal catalysts were oxidized prior to the analysis.

To investigate the chemical bonding states of photoelectrodes with different metal catalysts, X-ray photoelectron spectroscopy (XPS) was performed. The Ga $2p_{3/2}$ XPS spectra were deconvoluted into a major peak of the Ga-N bond (1116.8 eV) and a minor peak of the Ga-O bond (1118.0 eV) (Fig. 1d)[40]. Similarly, the N 1*s* XPS spectra could be separated into a major N-Ga bond (396.9 eV) and a minor N-H bond (398.5 eV), likely due to native oxide or hydroxide on the surface (Fig. 1e)[41]. It should be noted that although Co, Ni, or other catalysts were loaded on the GaN NWs, the intensities of the Ga $2p_{3/2}$ and N 1*s* spectra were almost preserved. This means that the metal catalysts were partially covered over the GaN and the GaN surface was still exposed. The Co catalysts exhibited Co^{2+} (782.7 and 798.3 eV) and Co^{3+} (781.2 and 796.8 eV) oxidation states in the Co *2p* spectrum (Fig. 1f). The Ni catalysts revealed Ni-O (853.5 and 871.1 eV), Ni-OH (854.7 and 872.3 eV), and their satellite bonds in the Ni *2p* spectrum (Fig. 1g)[42,43]. In the O 1 s XPS spectra, O-Co and O-Ni bonds from the oxidized phases of the catalysts were observed (Fig. 1h). This is in good agreement with the STEM-EDS results. The metal oxides were also formed on other metal catalysts, such as Pt, Ir, Rh, Pd, Cu, Ag, Ru, and Au (Figs. S3–S10), since the catalysts were deposited under aqueous conditions and exposed to ambient air prior to the analysis.

Photoelectrochemical NO_3^- reduction reaction

Photoelectrochemical (PEC) nitrate reduction to ammonia (NO_3^-RR) was performed in an H-type cell under AM1.5G 1-sun solar light. When light was illuminated on the n^+-p Si wafer through optically transparent GaN NWs, electrons and holes were generated in the conduction and valance bands of Si, respectively (Fig. 2a). The conduction bands of *n*-Si and *n*-GaN are approximately aligned[44], so the photogenerated electrons in *n*-Si spontaneously migrate to the conduction band of *n*-GaN by the built-in potential of the Si *p*-*n* junction. These photoelectrons then move to the metal catalysts and participate in reduction reaction. After the reaction was completed, the liquid products of NH_3, NO_2^-, and N_2H_4 in the cathodic compartment of the reactor were quantified through calibrated spectrocolorimetric measurements (Figs. S11–S13). The gas products were analyzed by gas chromatography.

In the electrolyte, a substantial number of water molecules coexist with NO_3^- ions. Therefore, when applying a cathodic potential to the photoelectrode, reduction reactions of NO_3^- conversion and hydrogen evolution may occur. To evaluate the photoelectrodes with respect to these two competing reactions, we performed linear sweep voltammetry (LSV) measurement of GaN/Si in 0.1 M K_2SO_4 with and without 0.5 M KNO_3 (Fig. S14). The onset potential (V_{onset}) at −1 mA/cm^2 for GaN/Si shifted positively from −0.63 to −0.21 V_{RHE} and the photocurrent density was as high as ~40 mA/cm^2 at −0.8 V_{RHE} when 0.5 M

https://doi.org/10.1038/s41467-025-58372-7

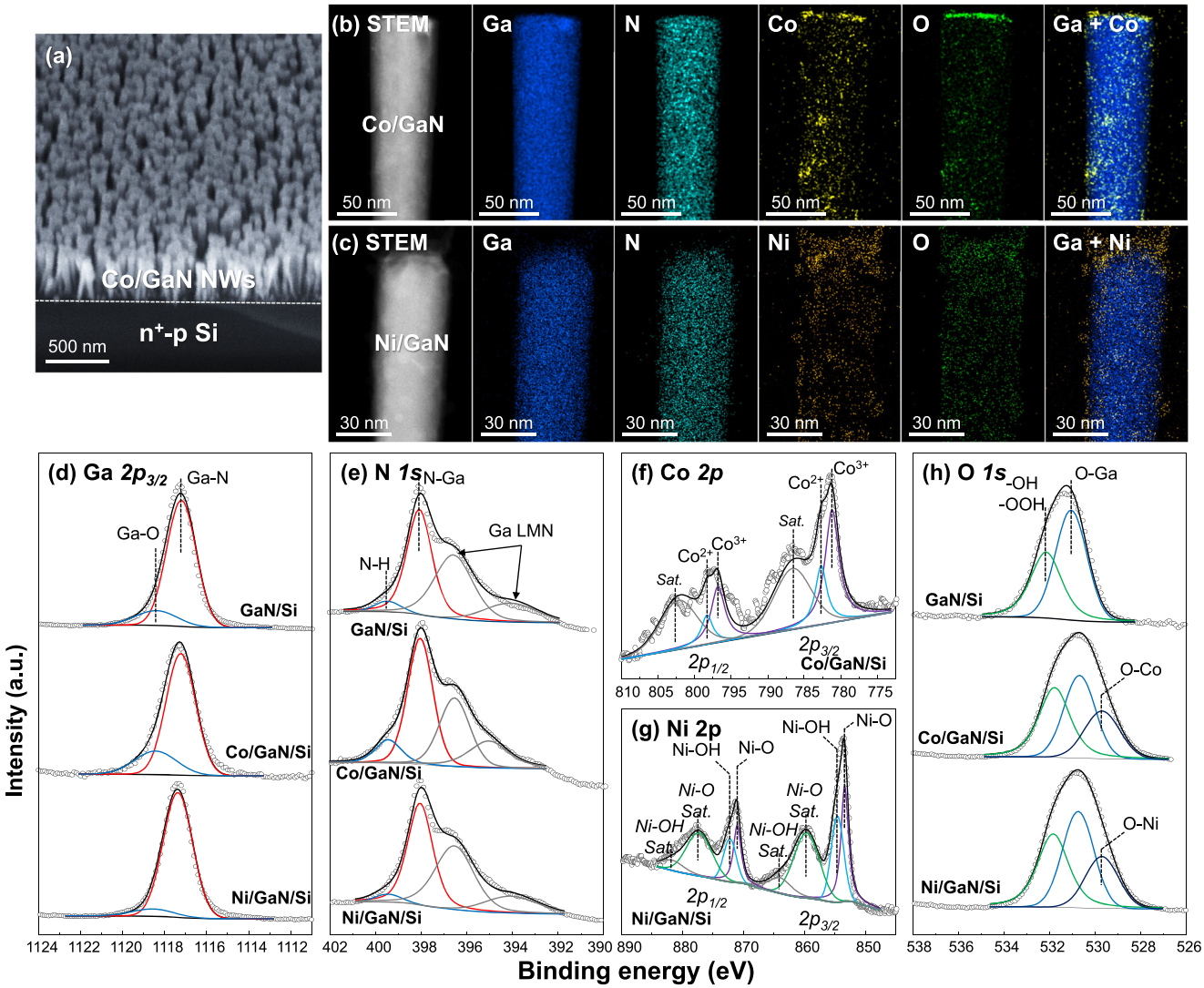

Fig. 1 | Material characterization of photoelectrodes. a 45 degree-tilt-view SEM image of Co/GaN/Si. STEM-HADDF images and EDS elemental maps of **b** Co/GaN and **c** Ni/GaN. Ga (blue) and N (cyan) were uniformly detected on GaN NWs while Co (yellow), Ni (orange), O (green) elements were segregated on the surface of GaN NWs. XPS spectra of **d** Ga $2p_{2/3}$, **e** N *1s*, **f** Co *2p*, **g** Ni *2p*, and **h** O 1*s* for GaN/Si, Co/GaN/Si, and Ni/GaN/Si.

KNO_3 was added to 0.1 M K_2SO_4. Moreover, GaN/Si exhibited fairly high FE_{NH3} = 61% at −0.7 V_{RHE}, suggesting that GaN surface is more catalytically active for NO_3^- reduction to NH_3 (NO_3^-RR) than for the hydrogen evolution reaction. However, Pt, Ir, and Rh catalysts (Figs. S15–S17) loaded on GaN/Si showed little difference in V_{onset} and photocurrent density regardless of NO_3^- in the electrolyte since these metals possess a high affinity for hydrogen adsorption rather than NO_3^- and good catalytic activity for hydrogen evolution reaction. As a result, these three metal catalysts showed very low faradaic efficiency of NH_3 (FE_{NH3}) <13% with high FE of H_2 (FE_{H2}) >80% at all potentials (0.3 to −0.8 V_{RHE}) (Fig. 2b). The photoelectrodes with Pd, Ag, Ru, and Cu catalyst showed FE_{NH3} of 37%, 41%, 60%, and 13%, respectively at −0.7 V_{RHE} (Figs. S18–S21). The predominant side product was NO_2^-, indicating the good catalytic activity in converting NO_3^- to NO_2^- compared to hydrogen evolution, but the further reduction to NH_3 was limited. Interestingly, when Au, Co, and Ni catalysts were coated on GaN/Si, the maximum FE_{NH3} can approach ~100% (Figs. S22–S24).

In more detail, GaN/Si selectively converted NO_3^- to NO_2^- at low potential (−0.1 V_{RHE}), with FE_{NO2^-} = 74% (Fig. 2c). As the potential was increased to −0.7 V_{RHE}, FE_{NO2^-} monotonically decreased to 35% and FE_{NH3} gradually increased to 61%. This demonstrated that GaN has excellent catalytic activity for the conversion of NO_3^- to NO_2^- and can further reduce NO_2^- to NH_3 under large cathodic potential. In the case of Cu catalysts supported on GaN/Si, NO_2^- was selectively produced (Fig. 2d) with high FE_{NO2^-} = 94% at 0.3 V_{RHE}. However, unlike GaN/Si, NO_2^- was still the major product (FE_{NO2^-} = 75%) with FE_{NH3} = 13% and FE_{N2H4} = 14% at −0.7 V_{RHE}. This suggests that the Cu catalyst coated on GaN has a negative effect on NH_3 synthesis by desorbing the NO_2^- intermediate from the surface and preventing further reduction of NO_2^-. This is discussed further in our theoretical analysis. In stark contrast, Co/GaN/Si dramatically improved FE_{NH3} to 72% and 99% at 0.3 and 0.2 V_{RHE}, respectively (Fig. 2e). These potentials are more positive than the standard reduction potential of NO_3^-, meaning that the photovoltage generated by GaN/n^+-*p* Si photoelectrode (~0.5 V)[37–39] biases the reduction reaction and shifts the operating potential window positively. At the large cathodic potential of −0.8 V_{RHE}, there was a decline of FE_{NH3} to 68% due to increase in the FE_{H2}. In contrast, Ni/GaN/Si selectively produced NH_3 over other competing reactions although Ni/GaN/Si required a more negative potential (0 V_{RHE}) to achieve FE_{NH3} > 90% (Fig. 2f). The total faradaic efficiency was less than 100% especially at anodic potentials (+0.2–0 V_{RHE}) because some electrons could be used for the reduction of NO_3^- to other nitrogen-containing species, such as N_2 and NO, which were not fully analyzed. Additionally, the non-faradaic capacitive current density from ionic adsorption and desorption at the

https://doi.org/10.1038/s41467-025-58372-7

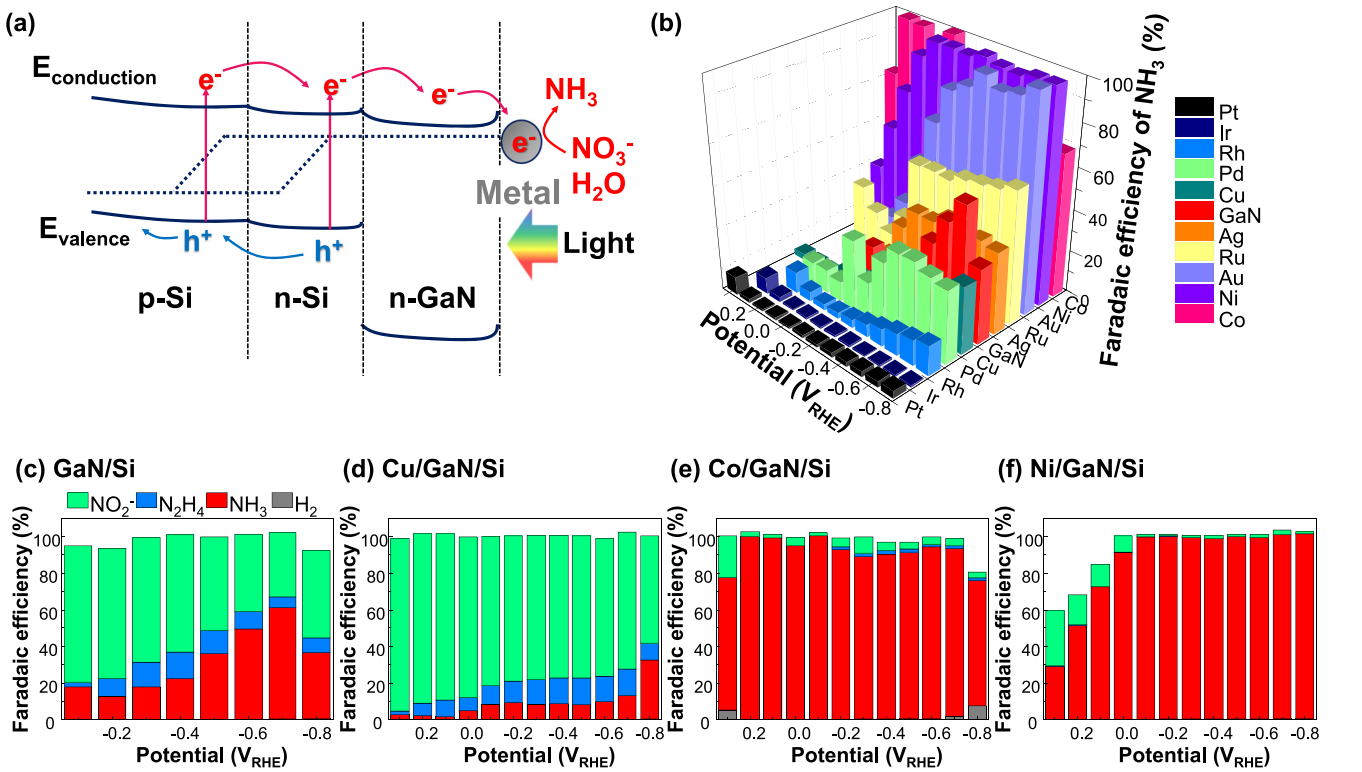

Fig. 2 | Catalyst-dependent photoelectrochemical nitrate reduction. a Energy band diagram of metal/GaN/Si photoelectrode under light illumination. **b** Faradaic efficiency of NH_3 for metal catalysts loaded on GaN/Si. The measurement was conducted in 0.1 M K_2SO_4 with 0.5 M KNO_3 at various cathodic potentials (0.3 to −0.8 V_{RHE}) under 1 sun light illumination. Faradaic efficiency of H_2, NH_3, NO_2^-, and N_2H_4 for **c** GaN/Si, **d** Cu/GaN/Si, **e** Co/GaN/Si, and **f** Ni/GaN/Si. Co and Ni catalysts showed the highest FE_{NH3} (>98%) among the tested samples.

electrical double layer could affect the derivation of faradaic efficiency. We further investigated the effects of the loading amount of metal catalysts coated on GaN NWs on catalytic properties (Fig. S25). Within the precursor concentration range in this work, there was no significant difference in catalytic performance, indicating that the determining factor for catalyst characteristics is the type of metal catalyst rather than the loading amount of metal catalysts.

To further study the metal-support interactions, we compared the LSV curves of n^+-p Si, GaN/Si, and metal catalysts loaded n^+-p Si and GaN/Si in 0.1 M K_2SO_4 with 0.5 M KNO_3 (Fig. 3a). In the order of Si, Co/Si, and Ni/Si, V_{onset} and photocurrent density were improved. GaN/Si showed a 1.1 V positive shift of V_{onset} compared to Si. Remarkably, GaN/Si loaded with Co and Ni catalysts showed much better V_{onset} = 0.22 and 0.27 V_{RHE}, respectively. Charge transfer kinetics from the photoelectrodes to reactants were investigated by the PEC impedance spectroscopy at 0 V_{RHE} under solar irradiation (Fig. 3b). The radius of the semicircle in the Nyquist plot correlates to the charge-transfer resistance during the PEC reaction[45]. For Si and Co/Si, the imaginary part of impedance diverged as the real part of impedance increased, indicating no faradaic charge transfer between the photoelectrode and the electrolyte. In contrast, for Ni/Si, GaN/Si, Co/GaN/Si, and Ni/GaN/Si, the radius of the semicircle decreased sequentially, implying a gradual reduction in charge transfer resistance. For GaN/Si, Co/GaN/Si, and Ni/GaN/Si photoelectrodes, the Nyquist plots were further analyzed at a more negative potential of −0.2 V_{RHE} (Fig. S26). Under this condition, the radius of the semicircle significantly reduced, indicating accelerated charge transfer under high bias. From the impedance results, the synergetic metal-GaN interaction facilitated the NO_3^- RR likely due to catalytic enhancement and increased electrochemical surface area (Fig. S27).

It should be noted that Co/GaN/Si showed the widest potential window (0.2 to −0.7 V_{RHE}) for the selective NH_3 production (FE_{NH3} > 90%) and Ni/GaN/Si also exhibited selective conversion of NO_3^- to NH_3 (FE_{NH3} > 90%) at potential ≤ 0 V_{RHE} (Fig. 3c). However, n^+-p Si (Fig. S28) and those with Co (Fig. S29) and Ni (Fig. S30) catalysts showed low FE_{NH3} < 54% with noticeably increased FE_{H2} > 42% or FE_{NO2-} >43% at −0.8 V_{RHE}. This clearly demonstrated that GaN NWs play an important role in reducing the overpotential and increasing the NH_3 selectivity of NO_3^- RR. Since Co/GaN/Si and Ni/GaN/Si exhibited the promising V_{onset} (>0.3 V_{RHE}), high photocurrent density (>38 mA/cm^2), and FE_{NH3} (~100%) over the wide potential window, high production rates of 17.5 and 83.3 μmol/h/cm^2 were achieved, respectively at 0 V_{RHE}. In addition, the maximum production rate of NH_3 = 166.7 μmol/h/cm^2 at −0.7 V_{RHE} and 201.6 μmol/h/cm^2 at −0.4 V_{RHE} were demonstrated, respectively (Fig. 3d). Applied bias photon-to-current efficiency (ABPE) was calculated for the tested photoelectrodes (Fig. S31). In the order of Si, Co/Si, Ni/Si, GaN/Si, Co/GaN/Si, and Ni/GaN/Si, the maximum ABPE gradually increased up to 2.41%, indicating that GaN NWs are the promising platforms for loading the metal catalysts and facilitating the NO_3^- RR. The higher ABPE and NH_3 production rate for Ni/GaN/Si over Co/GaN/Si originated from more positive flat band potential likely due to more efficient electron injection from GaN NWs to Ni catalysts and better alignment for electron transfer from the Ni catalyst to the reactants (Fig. S32). Transient photocurrent measurements were conducted to further investigate charge carrier dynamics of photoelectrode with and without catalyst (Fig. S33). The results revealed that Co/GaN/Si exhibited superior charge retention and reduced recombination compared to GaN/Si, suggesting the critical role of Co catalyst in improving charge transfer efficiency and sustaining PEC activity during NO_3^- RR.

https://doi.org/10.1038/s41467-025-58372-7

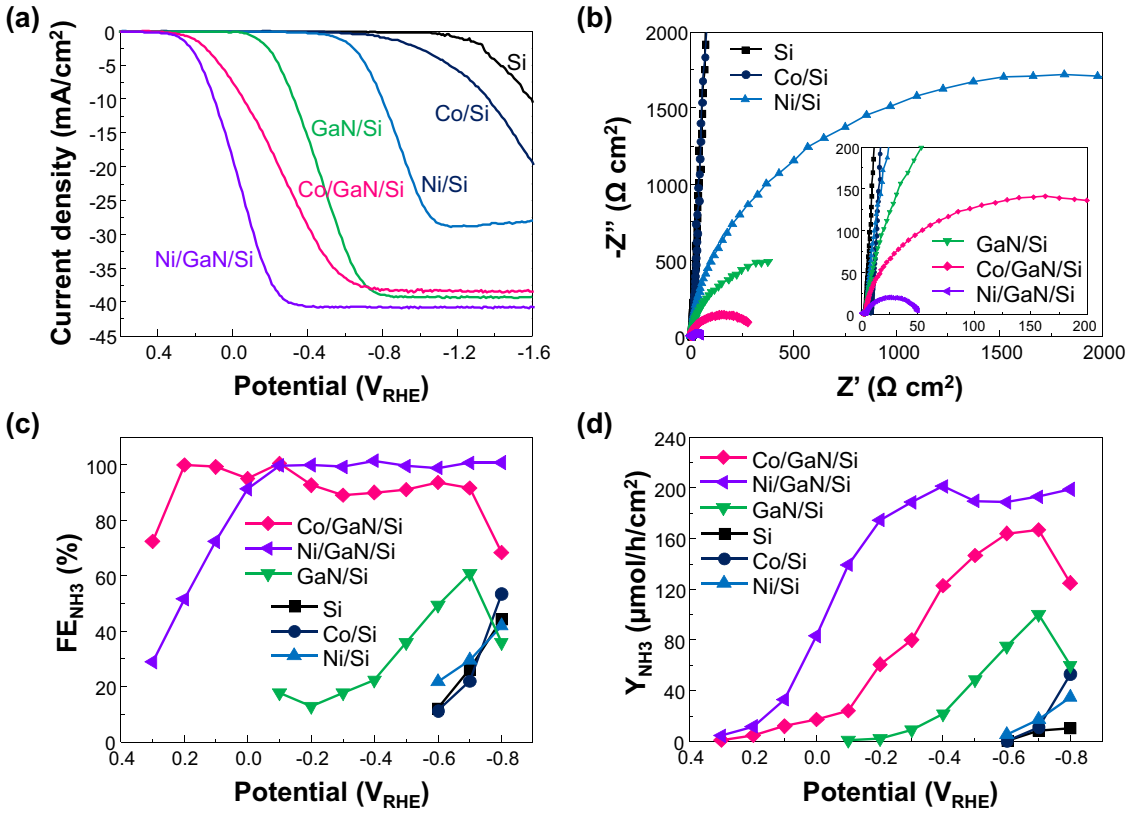

Fig. 3 | Effects of GaN NWs on photoelectrochemical nitrate reduction. a LSV curves and **b** Nyquist impedance plots of Si, Co/Si, Ni/Si, GaN/Si, Co/GaN/Si, and Ni/GaN/Si measured in 0.1 M K_2SO_4 with 0.5 M KNO_3 under 1 sun light illumination. **c** Faradaic efficiency and **d** production rate of NH_3 plotted as a function of cathodic potentials. Co/GaN/Si exhibited the widest potential window (−0.2 to −0.7 V_{RHE}) for high FE_{NH3} > 90% and Ni/GaN/Si revealed the best Y_{NH3} = 201.6 μmol/cm²/h at −0.4 V_{RHE}.

To investigate the influence of water dissociation in NO_3^-RR, we conducted kinetic isotopic effect (KIE) experiments by changing H_2O and D_2O in the electrolyte (Fig. S34). The KIE value was then calculated as the ratio of NH_3 production rates in electrolytes with H_2O and D_2O. For Co/Si, the KIE value was calculated at 1.63, indicating that the reaction was constrained by water dissociation[46]. Upon the introduction of GaN NWs, the KIE value for Co/GaN/Si significantly dropped to 1.15. Once protons became readily available at the surface through water dissociation by GaN NWs, it appears that Co catalysts efficiently reduce NO_3^- to NH_3 through deoxygenation and hydrogenation processes due to the intrinsic selectivity for producing NH_3 rather than hydrogen evolution. Consequently, using GaN nanowires as a support for metal catalysts presents a promising approach to demonstrating the synergy between proton supply and the catalysis of nitrogen-containing intermediates.

Control experiments in 0.1 M K_2SO_4 were carried out using Co/GaN/Si to confirm whether NH_3 is produced from NO_3^- reactant, and there was no NH_3 produced without NO_3^- in the electrolyte (Fig. S35). Moreover, ^{15}N isotope labeling clearly evidenced that $^{15}NH_3$ was produced from $^{15}NO_3^-$ (Fig. S36). The measured V_{onset}, FE_{NH3}, and Y_{NH3} of Co or Ni catalysts on GaN NWs were comparable to those of recent photoelectrodes and superior to state-of-the-art electrocatalysts for NO_3^-RR (Table S1).

To study the effects of metal catalysts on catalytic NO_3^-RR activity, in-situ Fourier transform infrared (FTIR) measurements were performed for two representative photoelectrodes of GaN/Si (Fig. S37) and Co/GaN/Si (Fig. 38). The potential-dependent spectra (−0.2 to −0.7 V_{RHE}, Figs. S37a, S38a) revealed distinct behaviors between the two photoelectrodes. As NO_3^-RR proceeded, both samples exhibited a gradual decrease in the peak intensity at 1348 cm^{-1} [47], which attributes to the consumption of NO_3^- ions in the solution. For GaN/Si (Fig. S37a), a characteristic band at 1230 cm^{-1} corresponding to NO_2^- intermediates, was clearly observed. This band became more pronounced at more negative potentials, indicating the accumulation of NO_2^- as a primary product. Time-resolved measurements at −0.5 V_{RHE} (Fig. S37b) further confirmed the buildup of NO_2^- near the surface as the intensity of NO_2^- band gradually increased over time. In contrast, Co/GaN/Si (Fig. S38a) demonstrated no signal of the NO_2^- band, even at highly cathodic potentials, suggesting efficient conversion of NO_2 intermediates. This trend was further supported by the time-resolved measurements (Fig. S38b), where the absence of the NO_2^- band highlighted the catalytic role of Co catalyst in facilitating the PEC NO_3^-RR to NH_3.

Stability of Co/GaN/Si and Ni/GaN/Si

We recorded the photocurrent density of Co/GaN/Si (Fig. 4a) and Ni/GaN/Si (Fig. 4b) at 0 and −0.6 V_{RHE} under solar irradiation. At 0 V_{RHE}, the reaction was conducted for 5 cycles in 0.1 M K_2SO_4 with 0.5 M KNO_3 and each cycle was performed for 1 h with repeated replacement of fresh electrolyte. At −0.6 V_{RHE}, 10 cycles of reactions were performed for 5 h. The average photocurrent densities of Co/GaN/Si were 3.5 mA/cm² at 0 V_{RHE} and 35.8 mA/cm² at −0.6 V_{RHE}. Ni/GaN/Si showed higher average photocurrent densities of 16.1 mA/cm² at 0 V_{RHE} and 39.2 mA/cm² at −0.6 V_{RHE}. Both Co/GaN/Si (Fig. 4c) and Ni/GaN/Si (Fig. 4d) showed very high FE_{NH3} > 91% for 10 h. Co/GaN/Si continuously produced NH_3 with Y_{NH3} = 18.0 and 162.6 μmol/cm²/h at 0 and −0.6 V_{RHE}, respectively. Ni/GaN/Si also consistently converted NO_3^- to NH_3 with Y_{NH3} = 73.5 μmol/cm²/h at 0 V_{RHE}. At −0.6 V_{RHE}, Y_{NH3} of Ni/GaN/Si was ~170 μmol/cm²/h. There was no noticeable degradation of catalytic activity or change of morphology during the reaction,

https://doi.org/10.1038/s41467-025-58372-7

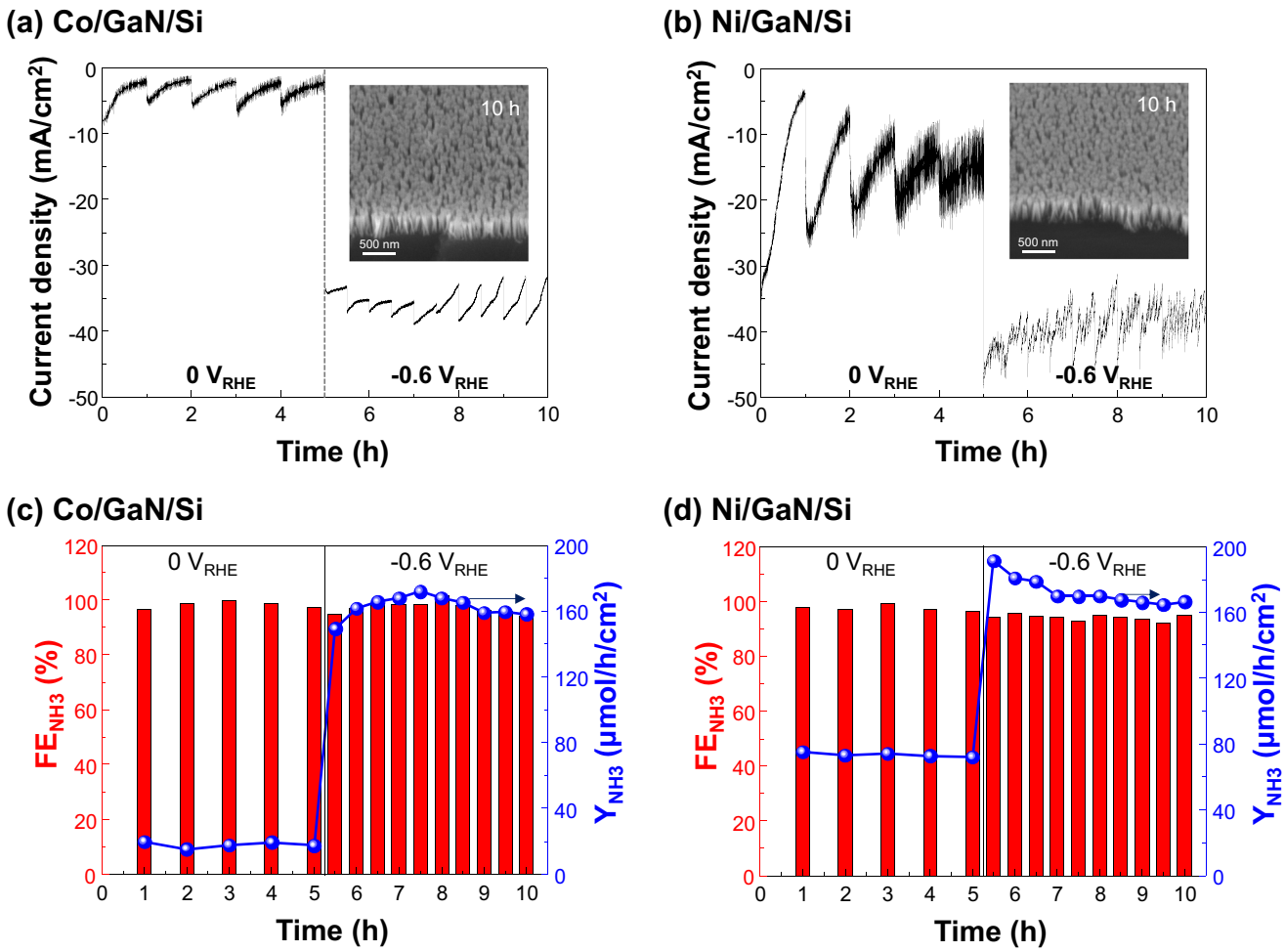

Fig. 4 | Stability test of photoelectrodes. Photocurrent density of **a** Co/GaN/Si and **b** Ni/GaN/Si in 0.1 M K_2SO_4 with 0.5 M KNO_3 under 1 sun light illumination. Measurements were performed 5 times at 0 V_{RHE} for 1 h each, and then 10 times at −0.6 V_{RHE} for 30 min each. Insets show SEM images of photoelectrodes after 10 h reaction. FE_{NH3} and Y_{NH3} for **c** Co/GaN/Si and **d** Ni/GaN/Si.

demonstrating that metal catalysts supported on GaN/Si photoelectrodes are promising platform for efficient and stable NO_3^-RR to NH_3. Evaluating the stability at high potential of −0.6 V_{RHE} is crucial from a material perspective since the accelerated degradation due to the detachment of metal catalysts from the photoelectrodes under harsh reaction conditions has been a significant issue[48]. The excellent stability of both Co/GaN/Si and Ni/GaN/Si highlights the potential advantage for designing a practical device.

Theoretical calculation

DFT investigations of the catalytic mechanism were performed to elucidate the origin of the different catalytic activities of Co and Cu catalysts for PEC NO_3^-RR. While the Cu catalyst maintains its metal character (see the XPS data in Fig. S7c that shows predominantly Cu^0), the Co derived cluster is oxidized to Co_3O_4 as seen in the XPS spectrum (Fig. 1f) which shows Co^{2+} and Co^{3+} peaks. The same holds true for Ni, where the XPS spectrum shows peaks for both Ni-O and Ni-OH (Fig. 1g). In addition to the mechanism on metallic Cu (Fig. S39 and Table S2) and Co (Fig. S40 and Table S3), we therefore performed a mechanistic study of NO_3^- reduction on Co_3O_4 (Figs. S41–S44 and Table S4) as well as NiOOH with Ni^{3+} and $Ni(OH)_2$ with Ni^{2+} (Figs. S45–S47 and Table S5).

The intermediates involved in the PEC process for Cu are shown in Fig. 5a, with the energetics of the preferred reaction path shown in Fig. 5b. The initial reduction of NO_3^- proceeds through oxidation of the surface and subsequent reductive removal of oxygen to regenerate the active material. The formal reactions in the PEC reduction of NO_3^- to NH_3 on a metal surface such as Cu and Co are given in Eqs. (1) to (11).

$$*NO_3^- + *H^+ + 2Me(0) \rightarrow *NO_2^- + (Me(I)_2OH)^+ \quad (1)$$

$$*NO_2^- + (Me(I)_2OH)^+ + H^+ + e^- \rightarrow *NO_2^- + Me(0) + Me(I)^+ + H_2O \quad (2)$$

$$*NO_2^- + Me(I)^+ + H^+ + e^- \rightarrow *NO_2^- + *H^+ + Me(0) \quad (3)$$

$$*NO_2^- + *H^+ + Me(0) \rightarrow *NO + Me(I)OH \quad (4)$$

$$*NO + Me(I)OH + H^+ + e^- \rightarrow *NO + Me(0) + H_2O \quad (5)$$

$$*NO + H^+ + e^- \rightarrow *NHO \quad (6)$$

$$*NHO + H^+ + e^- \rightarrow *NH_2O \quad (7)$$

$$*NH_2O + H^+ + e^- \rightarrow *NH_2OH \quad (8)$$

https://doi.org/10.1038/s41467-025-58372-7

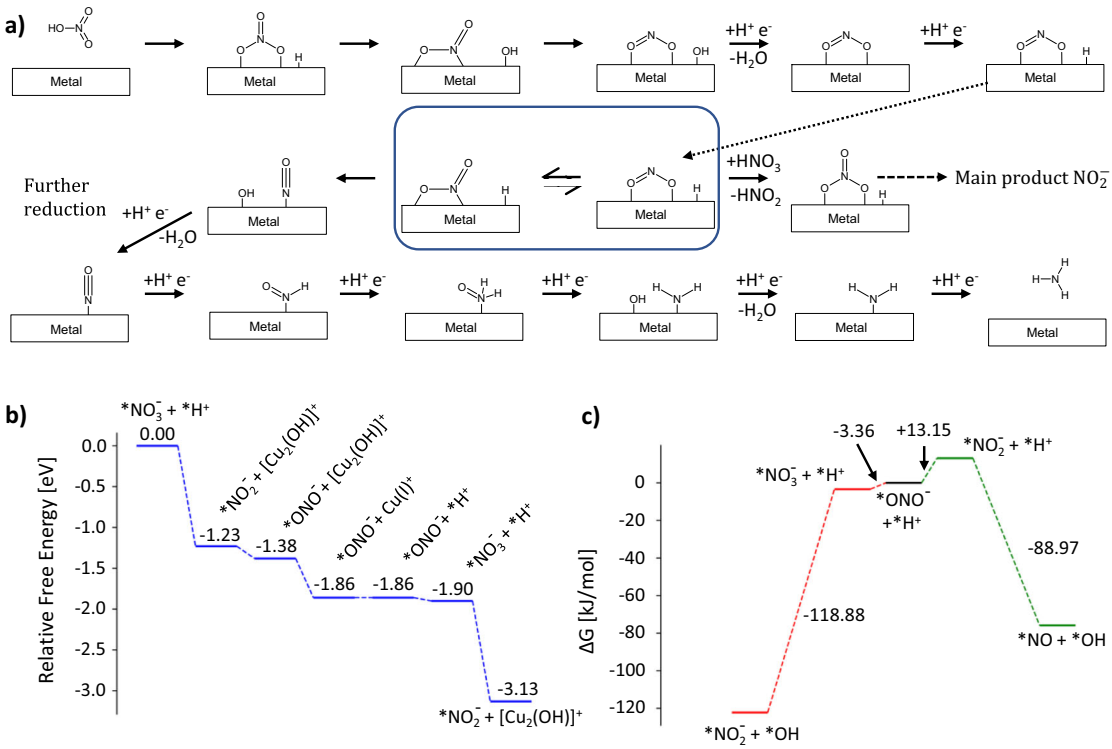

Fig. 5 | Main reaction pathways in the reduction of NO_3^- on Cu from DFT mechanistic study. a Full mechanism of NO_3^- reduction on the catalyst surfaces including reduction to NH_3 and incomplete reduction to NO_2^- and subsequent desorption. The key intermediate and its two binding modes determining the outcome are encircled. **b** Reduction from NO_3^- to NO_2^- and subsequent desorption on Cu catalyst. **c** Thermodynamics of desorption and further reduction through change of binding mode on Cu catalyst.

$$*NH_2OH + H^+ + e^- \rightarrow *NH_2 + H_2O \quad (9)$$

$$*NH_2 + H^+ + e^- + HNO_3 \rightarrow *NO_3^- + *H^+ + NH_3 \quad (10)$$

$$HNO_3 + 8H^+ + 8e^- \rightarrow NH_3 + 3H_2O \quad (11)$$

While the reduction of NO_3^- to NO_2^- is thermodynamically favorable on both metallic Cu and Co surfaces (Fig. 5b and S40, respectively), further reduction to the NO intermediate and subsequent NH_3 production depends on the thermal accessibility of the $*NO_2^-$ adsorption mode at this crucial intermediate. This thermal equilibrium between nonactive $*ONO^-$* and reactive $*NO_2^-$ adsorption modes, which does not involve an electron transfer and therefore cannot be supported by an applied potential, has different thermodynamic properties on Co and Cu catalysts. For the Cu catalyst, the NO_2^- intermediate prefers to bind to the surface in the $*ONO^-$* adsorption mode. However, for the second N = O bond dissociation and subsequent deoxygenation, the $*ONO^-$* mode must be switched to the $*NO_2^-$ adsorption mode. The switching to the $*NO_2^-$ mode on the Cu catalyst is highly endergonic, with a free energy change of 0.14 eV (=13.15 kJ/mol) (Fig. 5c). This means that the $*NO_2^-$ mode is not accessible on the Cu catalyst at room temperature and can only be generated as promoted by the energy released from the dissociation reaction. Furthermore, switching from the $*ONO^-$* mode to the $*NO_2^-$ adsorption mode is in competition with desorption of NO_2^- from the surface. This process of expulsion and replacement of the NO_2^- by an additional NO_3^- is slightly exergonic on Cu catalyst by −0.04 eV (=−3.36 kJ/mol). This much lower energy for the replacement of NO_2^- with NO_3^- in comparison to switching to the reactive $*NO_2^-$ intermediate mode explains why the main product of NO_3^-RR on Cu is NO_2^-. Once the NO_2^- is formed, it is much more likely to be desorbed rather than further reduction to NO through dissociation of the N = O bond.

For the oxidized species of Co_3O_4 and $Ni(OH)_2$, we found different reaction mechanism: reductive formation of defects which leads to the subsequent interaction with oxygen containing species, resulting in dissociation of N-O bond. This is different from the metal surfaces where dissociation of the N-O bond led to oxidation of the surface that needed to be reactivated by reduction. Therefore, the order of reaction, with first reducing the surface and then oxidizing it by reaction with the oxygen containing species is reversed on the oxidized species in comparison to the metallic surfaces. On the Co_3O_4, defect formation is favorable with −0.06 eV for first hydrogenation and −0.55 eV for water release under additional reduction (Fig. S42). Nitrate, nitrite, and NO can directly react with formed oxygen defects (Fig. S43). Notably, the $*ONO^-$* adsorption mode can dissociate since the defect can directly interact with the adsorbed oxygen. The reaction scheme and energetics of nitrate reduction on Co_3O_4 can be seen in Fig. 6, and the formal reactions in the PEC reduction of NO_3^- to NH_3 on Co_3O_4 are given in Fig. S44. Upon adsorption of nitrate on the surface, a defect is reductively formed, that reacts with the adsorbed NO_3^- to extract one oxygen, dissociating the first N-O bond and refilling the defect. This leads to $*NO_2$ on the surface, that gets reduced to NO_2^-. Further defect formation leads to dissociation of the second N-O bond, resulting in *NO. Further reduction of NO to NH_3 is thermodynamically downhill. Therefore, full reduction to NH_3 is the energetically favored pathway on Co_3O_4 catalyst, making NH_3 the main product.

As shown in Fig. S45, NiOOH readily reduces towards $Ni(OH)_2$ at low applied potentials, meaning the active species is most likely $Ni(OH)_2$ (Fig. S46). As $Ni(OH)_2$ has no active Ni surface sites available, oxygen defect formation is necessary for its reactivity. $Ni(OH)_2$ is a base that can be attacked by acids. The reaction mechanism determined by DFT is shown in Fig. 7a and the corresponding free energy

https://doi.org/10.1038/s41467-025-58372-7

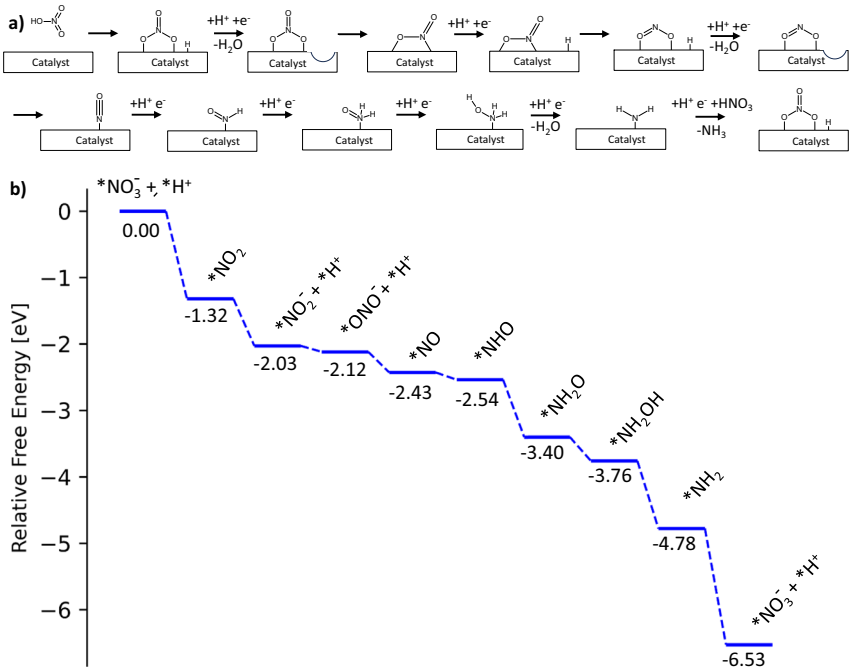

Fig. 6 | Reaction pathways in the reduction of NO_3^- on $Co3O_4$ from DFT mechanistic study. a Full mechanism of NO_3^- reduction on Co_3O_4. Defect formation leads to N-O bond dissociation. **b** Free energy of the reduction from NO_3^- to NH_3 on Co_3O_4.

profiles of the reaction steps are shown in Fig. 7b. HNO_3 can react with $Ni(OH)_2$, releasing water and leaving a positively charged surface with an oxygen defect. This defect directly interacts with the remaining nitrate to form the $Ni(OH)O^*NO_2$ intermediate with one of the oxygen atoms from nitrate being incorporated into the surface. Further reduction breaks the N-O bond, restoring the $Ni(OH)_2$ and releasing NO_2. Two NO_2 molecules can readily react with water and form HNO_3 and HNO_2. These can then interact with the surface again, releasing water and forming $Ni(OH)O^*NO$ species. Upon reduction, NO is released, followed by protonation and water release. The NO then reacts, forming $Ni(OH)O^*N$ intermediate that is subsequently reduced to $Ni(OH)O^*NH$ and $Ni(OH)O^*NH_2$. Continued reduction leads to release of NH_3, leaving behind a hydrogen defect that is filled in the next reduction step, completing the cycle. All steps are thermodynamically downhill with the exception of the release of NO that is 0.02 eV uphill- an energy easily provided by the photoexcited electrons. Therefore, the main product of nitrate reduction on $Ni(OH)_2$ is NH_3. The full reaction paths and energetics of reduction to NH_3 as well as reduction to NO_2^- and subsequent desorption for all catalytic systems are given in Figs. S39–S47 and summarized in Tables S2–S6.

Discussion

In summary, we have investigated various metal catalysts for the PEC NO_3^-RR to NH_3. Remarkably, we found that first-row earth-abundant transition metals Co and Ni catalysts outperformed noble metals (Pt, Ir, Rh, Pd, Ru, Au, and Ag) and the widely used Cu catalyst. In-situ IR measurement showed that a large number of NO_2^- intermediates were desorbed from Cu catalysts but further reduced to NH_3 on Co catalysts. Theoretical calculations confirmed that the deoxygenation process of the $^*NO_2^-$ intermediate is feasible on Co_3O_4 and $Ni(OH)_2$ catalysts via reaction with oxygen defects. In contrast, NO_2^- molecules desorbed from the Cu surface due to the $^*ONO^-{}^*$ binding mode with a lower barrier for desorption than for switching to the $^*NO_2^-$ mode that is needed for further deoxygenation processes. This leads to incomplete reduction of nitrate to nitrite on Cu, while the Co and Ni containing catalysts are capable of full reduction of NO_3^- to NH_3. Owing to the strong catalytic activities of Co and Ni and the synergistic effects of metal-GaN interactions, high performance was achieved, including a low onset potential $V_{onset} = 0.3\ V_{RHE}$, high faradaic efficiency of NH_3 (~99% at 0.2 V_{RHE}), and high production rate of NH_3 (201.6 μmol/h/cm^2 at −0.4 V_{RHE}). Moreover, the photoelectrodes were stable and performed for 10 h of reaction without any noticeable degradation. The photoelectrodes, which consist of the two most popular semiconductors (Si and GaN) and inexpensive transition metals (Co and Ni), have the potential to be used in industry-scale conversion of NO_3^- pollutant to value-added NH_3 under solar light.

Methods

Preparation of GaN nanowires on n$^+$-p Si wafer

Starting p-type Si (100) wafer was purchased from Purewafer and has a resistivity of 1–10 Ω·cm. The n$^+$-p Si was demonstrated by spin-coating of phosphorus dopant on the front side of the polished p-type Si wafer and then thermal annealing at 950 °C under nitrogen atmosphere for 4 h. N-type GaN NWs were grown on n$^+$-p Si wafer by plasma-assisted molecular-beam epitaxy under nitrogen-rich condition to promote the formation of an N-terminated surface. The growth temperature was 790 °C and the duration was ~2 h. The forward plasma power was 350 W with Ga flux beam equivalent pressure of 5×10^{-8} Torr.

Loading of metal catalysts on GaN/Si

Metal catalysts were loaded on GaN/Si by a photodeposition method. GaN/Si wafer on a Teflon holder was placed in the bottom of a quartz reactor containing 66 mL of 20 vol% methanol aqueous solution. Then, 10 μl of 0.2 M H_2PtCl_6 (Sigma-Aldrich, 99.9%), 0.2 M $IrCl_3$ (Sigma-Aldrich, 99.8%), 0.2 M Na_3RhCl_6 (Sigma-Aldrich), 0.1 M K_2PdCl_4 (Sigma-Aldrich, 99.99%), 0.2 M $CuCl_2$ (Sigma-Aldrich, 99.999%), 0.2 M $AgNO_3$ (Sigma-Aldrich, ≥99.0%), 0.4 M $RuCl_3$ (Sigma-Aldrich, 99.99%), 0.2 M $HAuCl_4$ (Sigma-Aldrich, 99.99%), 0.2 M $Ni(NO_3)_2$ (Sigma-Aldrich, 99.999%), or 0.2 M $CoCl_2$ (Sigma-Aldrich, 97%) solutions were added into the chamber to deposit Pt, Ir, Rh, Pd, Cu, Ag, Ru, Au, Ni, or Co catalysts, respectively. The reactor was evacuated for 5 min using a rotary pump. A 300 W Xe lamp (Cermax,

https://doi.org/10.1038/s41467-025-58372-7

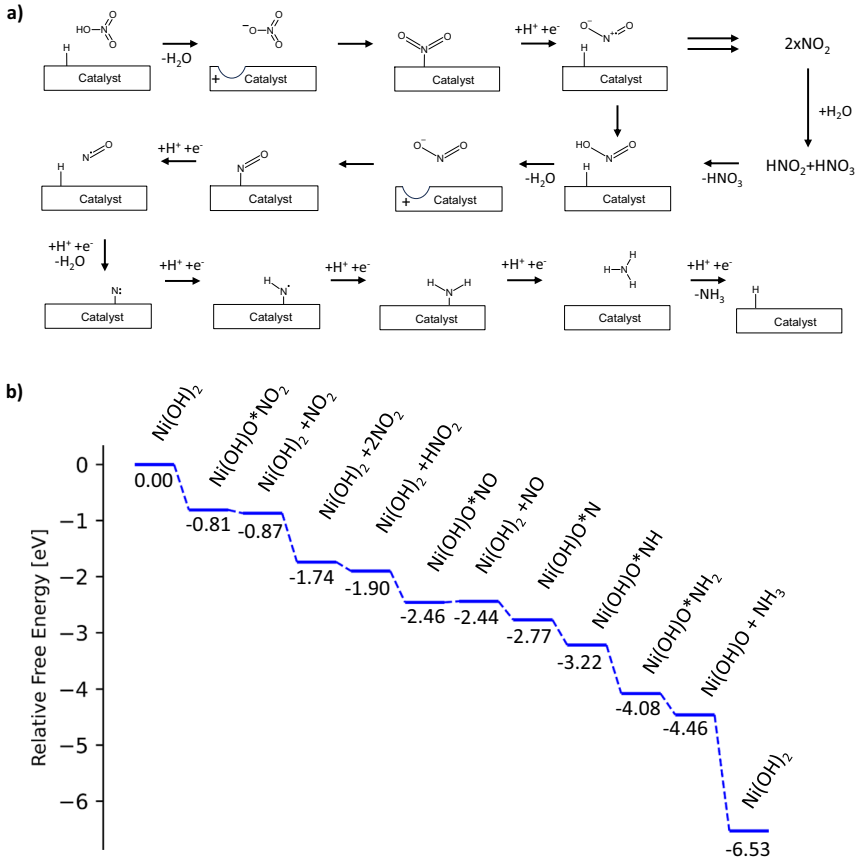

Fig. 7 | Reaction pathways in the reduction of NO_3^- on $Ni(OH)_2$ from DFT mechanistic study. a Mechanism of NO_3^- reduction to NH_3 on $Ni(OH)_2$. Defect formation allows for attachment of nitrate, further reduction regenerates the $Ni(OH)_2$ surface and dissociates the N-O bond. The mechanism proceeds similarly with HNO_2 and NO, with full reduction towards NH_3. **b** Free energy of the NO_3^- reduction on $Ni(OH)_2$.

PE300BUV) was used as a light source which irradiated the chamber for 30 min. When light illuminated the GaN/Si wafer in the precursor solution, electrons are photoexcited to the conduction band, creating holes in the valence band of the GaN NWs. The photoexcited electrons then migrated to the GaN surface, participating in the reduction of metal ions. Simultaneously, photogenerated holes in the valence band migrated to the surface, oxidizing the methanol sacrificial agent in the solution. Since the bandgap of GaN (~3.4 eV) was suitable to absorb ultraviolet light and drive the redox reactions, there was no need for an external bias in the photodeposition process. After the photodeposition, the samples were rinsed with deionized water and dried by air blowing.

Characterization

The scanning electron microscopy (SEM) was performed using a field-emission scanning electron microscope (MIRA3 TESCAN) with 10 kV acceleration voltage. The high-angle annular dark-field scanning-transmission electron microscopy (HAADF-STEM) and energy dispersive X-ray spectroscopy (EDS) images were collected at 200 kV using JEOL 3100R05 Double Cs Corrected TEM/STEM with a 200 kV accelerating voltage. The X-ray photoelectron spectroscopy (XPS) was measured using a Kratos Axis Ultra XPS with a monochromatic Al Kα source. The ultraviolet-visible (UV-vis) spectroscopy (Varian 50-Bio) was used to quantify the products in the electrolytes. The In-situ Fourier transform infrared spectroscopy was performed on an INVENIO-R Fourier transform infrared spectrometer (FTIR) equipped with a mercury cadmium telluride (MCT) detector. Isotope labeling test was performed by ^1H nuclear magnetic resonance (NMR) measurment using Varian Vnmrs 500. 525 µL of solution was mixed with 50 µl of 0.5 M H_2SO_4 (Sigma-Aldrich, 95.0–98.0%), 50 µl of DMSO-d_6 (Sigma-Aldrich, 99.9%), 25 µl of 12.5 mM maleic acid (Sigma-Aldrich, ≥99%), and 25 µl of 27 mM Gd^{3+} solution (Sigma-Aldrich, 99.9%) for NMR analysis[49].

Photoelectrochemical NO_3^- reduction

All photoelectrochemical measurements were performed in an H-type cell separated by a Nafion membrane with a three-electrode system using a potentiostat (Bio Logic SAS SP-200). Ag/AgCl filled with 3 M KCl was used for the reference electrode and Pt wire was used for the counter electrode. GaN/Si as well as other metal-loaded photoelectrodes were used as the working electrodes. The measured potentials ($V_{Ag/AgCl}$) (V) were converted to the reversible hydrogen electrode (V_{RHE}) (V) by using the Nernst function: $V_{RHE} = V_{Ag/AgCl} + 0.197 + 0.0591 \times pH$. The electrolytes were aqueous solutions of 0.1 M K_2SO_4 (Sigma-Aldrich, ≥99%) or 0.1 K_2SO_4 with 0.5 M KNO_3 (Sigma-Aldrich, ≥99%) prepared by dissolving the solid salts in deionized water. pH values of electrolytes were measured using a pH meter (Mettler Toledo). 8 ml of electrolyte was filled in the cathodic compartment of H-type cell and purged with Ar for 30 min before the measurement. The light source for the photoelectrochemical reaction was LCS-100 (ORIEL) and the intensity with AM 1.5G filter was calibrated by adjusting the distance from the sample to the light source. Linear sweep voltamnetry curves were obtained at a rate of 10 mV/s. Chronoamerometic curves were recorded every 1 s. All measurements were conducted at ambient pressure and room temperature. After the reaction, gas products were analyzed using gas chromatography (Shimadzu GC-8A) equipped with a thermal conductivity detector. Then, the electrolytes were collected to quantify the NH_3, NO_2^-, and N_2H_4 products using UV-Vis spectrophotometry.

Determination of NH_3

The concentration of NH_3 product was spectrocolorimetrically determined by the indophenol blue method[25]. 1 ml of electrolyte was taken out from the cathodic compartment in H-typce cell (and diluted if needed). Then, 1 ml of a 1 M NaOH (Sigma-Aldrich, ≥97%) solution containing 5 wt% salicylic acid (Sigma-Aldrich, ≥99%) and 5 wt% sodium citrate (Sigma-Aldrich, ≥99%) was added to the 1 ml of electrolyte, followed by the addition of 0.5 ml of 0.05 M NaClO (Sigma-Aldrich, available chlorine 4.00–4.99%) and 0.1 ml of 1 wt% $C_5FeN_6Na_2O$ (Sigma-Aldrich, ≥99%) solution. The solution was stored in dark for ~2 h at room temperature before the UV-vis measurement. The concentration of NH_3 was determined by absorbance at a wavelength of 655 nm. NH_4Cl (Sigma-Aldrich, ≥99.5%) standard solutions with known concentration was used for the calibration.

Determination of NO_2^-

0.2 g of N-(1-naphthyl) ethylenediamine dihydrochloride (Sigma-Aldrich, ≥98%), 4 g of p-aminobenzenesulfonamide (Sigma-Aldrich, ≥98%), and 10 ml of phosphoric acid (Sigma-Aldrich, ≥85 wt% in H_2O) were dissolved into 50 ml of deionized water as the color reagent[25]. Then, 2.5 ml of the diluted electrolyte were mixed with 0.05 ml of color reagent and stored ~30 min prior to the measurement. The absorbance at a wavelength of 540 nm was collected by UV-vis spectrometer to quantify the concentration of NO_2^-. KNO_2 (Sigma-Aldrich, ≥96%) standard solutions with known concentration was used for the calibration.

Determination of N_2H_4

1.5 g of $C_9H_{11}NO$ (Sigma-Aldrich, 97%) and 7.5 ml of HCl (Sigma-Aldrich, 37%) were added into 75 ml of ethanol (Sigma-Aldrich, ≥99.5%) as the color agent[50]. Then, 1 ml of the electrolyte was mixed with 1 mL of color reagent and stored for ~1 h before the measurment. The absorbance at a wavelength of 455 nm was collected by UV-vis spectrometer to determinte the concentration of N_2H_4. Hydrazine hydrate (Sigma-Aldrich, 80% in water) standard solutions with known concentration was used for the calibration.

Data availability

Data supporting the findings of this study are available within the article and supplementary information. A source data file for data presented in the main text is provided with the manuscript. All other data supporting the findings are available from the corresponding authors upon request. Source data are provided with this paper.

References

1. van Langevelde, P. H., Katsounaros, I. & Koper, M. T. Electrocatalytic nitrate reduction for sustainable ammonia production. *Joule* **5**, 290–294 (2021).
2. Rogan, W. J. & Brady, M. T. Committee on Environmental Health, and the Committee on Infectious Diseases. Drinking water from private wells and risks to children. *Pediatrics* **123**, e1123–e1137 (2009).
3. Martínez, J., Ortiz, A. & Ortiz, I. State-of-the-art and perspectives of the catalytic and electrocatalytic reduction of aqueous nitrates. *Appl Catal. B* **207**, 42–59 (2017).
4. MacFarlane, D. R. et al. A roadmap to the ammonia economy. *Joule* **4**, 1186–1205 (2020).
5. Soloveichik, G. Electrochemical synthesis of ammonia as a potential alternative to the Haber–Bosch process. *Nat. Catal.* **2**, 377–380 (2019).
6. Wang, P. et al. Breaking scaling relations to achieve low-temperature ammonia synthesis through LiH-mediated nitrogen transfer and hydrogenation. *Nat. Chem.* **9**, 64–70 (2017).
7. Chen, G. F. et al. Advances in electrocatalytic N2 reduction—strategies to tackle the selectivity challenge. *Small Methods* **3**, 1800337 (2019).
8. Zhang, G. et al. Tandem electrocatalytic nitrate reduction to ammonia on MBenes. *Angew. Chem. Int Ed.* **62**, e202300054 (2023).
9. Li, J. et al. Efficient ammonia electrosynthesis from nitrate on strained ruthenium nanoclusters. *J. Am. Chem. Soc.* **142**, 7036–7046 (2020).
10. Song, Z. et al. Efficient electroreduction of nitrate into ammonia at ultra-low concentrations via enrichment effect. *Adv. Mater.* **34**, 2204306 (2022).
11. Wang, Y. et al. Enhanced nitrate-to-ammonia activity on copper–nickel alloys via tuning of intermediate adsorption. *J. Am. Chem. Soc.* **142**, 5702–5708 (2020).
12. Liu, H. et al. Efficient electrochemical nitrate reduction to ammonia with copper-supported rhodium cluster and single-atom catalysts. *Angew. Chem.* **7**, e202202556 (2022).
13. Ge, Z. X. et al. Interfacial engineering enhances the electroactivity of frame-like concave RhCu bimetallic nanocubes for nitrate reduction. *Adv. Energy Mater.* **12**, 2103916 (2022).
14. Chen, G.-F. et al. Electrochemical reduction of nitrate to ammonia via direct eight-electron transfer using a copper–molecular solid catalyst. *Nat. Energy* **5**, 605–613 (2020).
15. Wang, Y., Zhou, W., Jia, R., Yu, Y. & Zhang, B. Unveiling the activity origin of a copper-based electrocatalyst for selective nitrate reduction to ammonia. *Angew. Chem. Int Ed.* **59**, 5350–5354 (2020).
16. Li, J. et al. 3.4% solar-to-ammonia efficiency from nitrate using fe single atomic catalyst supported on MoS2 nanosheets. *Adv. Funct. Mater.* **32**, 2108316 (2022).
17. Kani, N. C. et al. Solar-driven electrochemical synthesis of ammonia using nitrate with 11% solar-to-fuel efficiency at ambient conditions. *Energy Environ. Sci.* **14**, 6349–6359 (2021).
18. He, W. et al. Splicing the active phases of copper/cobalt-based catalysts achieves high-rate tandem electroreduction of nitrate to ammonia. *Nat. Commun.* **13**, 1–13 (2022).
19. Zhang, N. et al. Governing interlayer strain in bismuth nanocrystals for efficient ammonia electrosynthesis from nitrate reduction. *ACS Nano* **16**, 4795–4804 (2022).
20. Ye, S. et al. Elucidating the activity, mechanism and application of selective electrosynthesis of ammonia from nitrate on cobalt phosphide. *Energy Environ. Sci.* **15**, 760–770 (2022).
21. Jiang, M. et al. Interfacial reduction nucleation of noble metal nanodots on redox-active metal–organic frameworks for high-efficiency electrocatalytic conversion of nitrate to ammonia. *Nano Lett.* **22**, 2529–2537 (2022).
22. Liu, Q. et al. Ambient ammonia synthesis via electrochemical reduction of nitrate enabled by NiCo2O4 nanowire array. *Small* **18**, 2106961 (2022).
23. Cheng, X. F. et al. Coordination symmetry breaking of single atom catalysts for robust and efficient nitrate electroreduction to ammonia. *Adv. Mater.* **34**, 2205767 (2022).
24. Sun, W. J. et al. Built-in electric field triggered interfacial accumulation effect for efficient nitrate removal at ultra-low concentration and electroreduction to ammonia. *Angew. Chem. Int Ed.* **60**, 22933–22939 (2021).
25. Wu, Z.-Y. et al. Electrochemical ammonia synthesis via nitrate reduction on Fe single atom catalyst. *Nat. Commun.* **12**, 1–10 (2021).
26. Li, P., Jin, Z., Fang, Z. & Yu, G. A single-site iron catalyst with pre-occupied active centers that achieves selective ammonia electrosynthesis from nitrate. *Energy Environ. Sci.* **14**, 3522–3531 (2021).
27. Li, X., Shen, P., Li, X., Ma, D. & Chu, K. Sub-nm RuO x clusters on Pd metallene for synergistically enhanced nitrate electroreduction to ammonia. *ACS Nano* **17**, 1081–1090 (2023).
28. Kim, H. E. et al. Photoelectrochemical nitrate reduction to ammonia on ordered silicon nanowire array photocathodes. *Angew. Chem. Int Ed.* **134**, e202204117 (2022).

29. Ren, S. et al. Enhanced charge-carrier dynamics and efficient photoelectrochemical nitrate-to-ammonia conversion on antimony sulfide-based photocathodes. *Angew. Chem. Int. Ed.* **63**, e202409693 (2024).
30. Ren, S., Gao, R. T., Nguyen, N. T. & Wang, L. Enhanced charge carrier dynamics on Sb2Se3 photocathodes for efficient photoelectrochemical nitrate reduction to ammonia. *Angew. Chem.* **136**, e202317414 (2024).
31. van Deelen, T. W., Hernández Mejía, C. & de Jong, K. P. Control of metal-support interactions in heterogeneous catalysts to enhance activity and selectivity. *Nat. Catal.* **2**, 955–970 (2019).
32. Dong, W. J. et al. Tailoring electronic structure of bifunctional Cu/Ag layered electrocatalysts for selective CO2 reduction to CO and CH4. *Nano Energy* **78**, 105168 (2020).
33. Shi, L., Yin, Y., Wang, S. & Sun, H. Rational catalyst design for N2 reduction under ambient conditions: strategies toward enhanced conversion efficiency. *ACS Catal.* **10**, 6870–6899 (2020).
34. Wang, S. et al. High-throughput identification of highly active and selective single-atom catalysts for electrochemical ammonia synthesis through nitrate reduction. *Nano Energy* **100**, 107517 (2022).
35. Parastaev, A. et al. Boosting CO2 hydrogenation via size-dependent metal–support interactions in cobalt/ceria-based catalysts. *Nat. Catal.* **3**, 526–533 (2020).
36. Zhang, J., Zhang, Q. & Feng, X. Support and interface effects in water-splitting electrocatalysts. *Adv. Mater.* **31**, 1808167 (2019).
37. Dong, W. J. et al. Pt nanoclusters on GaN nanowires for solar-asssisted seawater hydrogen evolution. *Nat. Commun.* **14**, 179 (2023).
38. Xiao, Y. et al. Oxynitrides enabled photoelectrochemical water splitting with over 3000 hrs stable operation in practical two-electrode configuration. *Nat. Commun.* **14**, 2047 (2023).
39. Xiao, Y. et al. Crystallographic effects of GaN nanostructures in photoelectrochemical reaction. *Nano Lett.* **22**, 2236–2243 (2022).
40. Wolter, S. et al. X-ray photoelectron spectroscopy and x-ray diffraction study of the thermal oxide on gallium nitride. *Appl Phys. Lett.* **70**, 2156–2158 (1997).
41. Duan, T., Pan, J. & Ang, D. S. Interfacial chemistry and valence band offset between GaN and Al2O3 studied by X-ray photoelectron spectroscopy. *Appl Phys. Lett.* **102**, 201604 (2013).
42. Chastain, J. & King, R. C. Jr Handbook of X-ray photoelectron spectroscopy. *Perkin Elmer Corp.* **40**, 221 (1992).
43. Weidler, N. et al. X-ray photoelectron spectroscopic investigation of plasma-enhanced chemical vapor deposited NiO x, NiO x (OH) y, and CoNiO x (OH) y: influence of the chemical composition on the catalytic activity for the oxygen evolution reaction. *J. Phys. Chem. C.* **121**, 6455–6463 (2017).
44. Vanka, S. et al. High efficiency Si photocathode protected by multifunctional GaN nanostructures. *Nano Lett.* **18**, 6530–6537 (2018).
45. Dong, W. J. et al. Silver halide catalysts on GaN nanowires/Si heterojunction photocathodes for CO2 reduction to syngas at high current density. *ACS Catal.* **12**, 2671–2680 (2022).
46. Deng, W., Zhang, P., Seger, B. & Gong, J. Unraveling the rate-limiting step of two-electron transfer electrochemical reduction of carbon dioxide. *Nat. Commun.* **13**, 803 (2022).
47. Pérez-Gallent, E., Figueiredo, M. C., Katsounaros, I. & Koper, M. T. Electrocatalytic reduction of Nitrate on Copper single crystals in acidic and alkaline solutions. *Electrochim. Acta* **227**, 77–84 (2017).
48. Tan, J. et al. Hydrogel protection strategy to stabilize water-splitting photoelectrodes. *Nat. Energy* **7**, 537–547 (2022).
49. Kolen, M., Smith, W. A. & Mulder, F. M. Accelerating 1H NMR detection of aqueous ammonia. *ACS Omega* **6**, 5698–5704 (2021).
50. Watt, G. W. & Chrisp, J. D. Spectrophotometric method for determination of hydrazine. *Anal. Chem.* **24**, 2006–2008 (1952).

Acknowledgements

This work was supported by United States Army Research Office Award W911NF2110337, awarded to V.S.B. and Z.M. The authors wish to thank Dr. Peng Zhou for discussions on the catalytic reactions.

Author contributions

W.J.D. conducted the photoelectrochemical tests. J.P.M. and Z.L. performed the DFT calculations. V.S.B. and Z.M. supervised the project. K.L. conducted photoelectrochemical analysis. Z.Y. performed XPS and TEM measurement. I.A.N. performed MBE growth. Y.X. discussed the catalytic reactions. K.R.Y. performed initial calculations and discussed possible catalytic mechanisms. W.J.D., J.P.M., V.S.B., and Z.M. wrote the manuscript. All authors discussed the results and commented on the manuscript.

Competing interests

Some IP related to this work was licensed to NS Nanotech, Inc. and NX Fuels, Inc., which were co-founded by Z.M. The University of Michigan and MI have a financial interest in the company. The remaining authors declare no competing interests.

Additional information

Supplementary information The online version contains supplementary material available at https://doi.org/10.1038/s41467-025-58372-7.

Correspondence and requests for materials should be addressed to Victor S. Batista or Zetian Mi.

Peer review information *Nature Communications* thanks Wooseok Yang, Lei Wang and the other, anonymous, reviewers for their contribution to the peer review of this work. A peer review file is available.